

*Submitted to the International Journal of Heat and Mass Transfer, April 7, 2021*

## **An Optimized Self-Adaptive Thermal Radiation Turn-Down Coating with Vanadium Dioxide Nanowire Array**

Ken Araki & Richard Z. Zhang\*

*Department of Mechanical Engineering, University of North Texas, Denton, 76207, USA.*

**ABSTRACT:** High performance metasurfaces for thermal radiative cooling applications can be identified using computational optimization methods. This work has identified an easy-to-fabricate temperature phase transition VO<sub>2</sub> nanowire array laid atop dielectric BaF<sub>2</sub> Fabry-Perot cavity-on-metal with total coating thickness of 2 μm. This optimized structure has ability to self-adaptively switch between high reflectance at low temperature to high emissivity at high temperature in the broad thermal infrared spectrum. This design demonstrates exceptional turn-down figure-of-merit compared to previously realized configurations utilizing VO<sub>2</sub> metasurfaces and multilayers. The mechanism is achieved with a sub-wavelength nanowire array effective medium that switches between anti-reflecting gradient coating and Fabry-Perot interference. This thin metasurface coating could impact self-cooling of the solar cells, batteries, and electrical devices where risk presents at high temperatures.

---

\* Corresponding author: zihao.zhang@unt.edu (R. Z. Zhang).

## Nomenclature

$b$	space between nanowires, $\mu\text{m}$
$d$	thickness, $\mu\text{m}$
DCM	Daytime Cooling Merit
$\mathbf{E}$	electric field vector
$f$	phase transition filling ratio
FOM	Turn-Down Figure of Merit
$h$	nanowire height, $\mu\text{m}$ ,
$\hbar$	reduced Planck's constant [J·s]
$I$	radiative intensity or solar irradiance, $\text{W}/\text{sr}\cdot\text{m}^2/\mu\text{m}$
$k_B$	Boltzmann constant, J/K
$n$	refractive index
$N$	number of samples
$P$	radiative power, $\text{W}/\text{m}^2$
PDD	power dissipation density, $\text{W}/\text{m}^3$
$\mathbf{r}$	randomization array
$T$	temperature, K
$w$	width of the nanowire, $\mu\text{m}$
$W$	width of the temperature range of metal-insulator transition, K

### *Greek symbols*

$\varepsilon$	emissivity
$\phi$	filling ratio
$\varphi$	azimuthal angle, deg
$\theta$	incident angle, deg
$\kappa$	extinction coefficient
$\Lambda$	period, $\mu\text{m}$
$\lambda$	wavelength, $\mu\text{m}$
$\omega$	angular frequency, rad/s
$\rho$	reflectivity
$\tau$	transmissivity

### *Subscripts*

0	vacuum / center value
AM1.5	air mass coefficient 1.5
BB	black body
coat	coating
con	combined convection and conduction heat transfer
cool	cooling
D	dielectric
EMT	effective medium theory
h	halfway through meta-insulator transition
i	insulator
m	metal
TE	transverse electric
TM	transverse magnetic

# 1 1. INTRODUCTION

2       Optical properties of thin films can be manipulated by introducing multilayered nano-patterns  
3 or periodic nanoelements that interface with electromagnetic waves from the visible to infrared.  
4 Various flavors of engineered nanoscale coatings include sub-diffraction plasmonic gratings [1-  
5 3], ultra-high reflection high contrast gratings [4-6], traditional diffraction gratings [7], and simple  
6 multilayers such as Fabry-Perot quarter-wave layers [8-10]. Among the considered, these  
7 nanoscale metasurfaces are potentially useful in photovoltaic device improvement and thermal  
8 emission regulation [11-14]. Yet the key attribute to be sought after is thermochromic tuning – the  
9 ability to change optical properties with engineered surface temperature – which may result in self-  
10 cooling amid temperature or environmental changes. Temperature phase change materials, such  
11 as vanadium dioxide ( $\text{VO}_2$ ) [9, 15, 16],  $\text{SmNiO}_3$  [17, 18],  $\text{Ti}_3\text{O}_5$  [19], and many others can tailor  
12 the optical properties when things get heated.

13        $\text{VO}_2$  integrated in photonic multilayers and gratings have demonstrated thermal radiative  
14 switching [9, 15, 20] A common coating design utilizes the concept of Fabry-Perot cavity  
15 interference to obtain low emittance when cool and high emittance at hot [9]. More complex  
16 multilayers can be added, for the purpose of daytime radiative cooling, as absorption to solar  
17 radiation is minimized compared to the emission in the infrared [15]. Other designs have patterned  
18 at-wavelength size scale cylindrical gratings [21, 22]. So far, the turn-down thermal performance  
19 of such coatings has been less than anticipated. The optimal thermochromic metastructure needs  
20 to be designed by weighting the Planck blackbody distribution at the corresponding wavelengths  
21 and temperatures close to the phase transition, as determined by Wien's displacement law. This  
22 work also considers the optimized structure that is easily feasible for nano/micro-fabrication, for  
23 a future in large scale-produced flexible radiative cooling blankets.

24       This work proposes a high turn-down grating by computational optimization of  $\text{VO}_2$  nanowires  
25 in a thin film.  $\text{VO}_2$  has a phase transition temperature at 340 K [14, 23, 24], where the phonon-  
26 electron structure transforms from insulating to metallic at temperatures above this transition  
27 temperature [25]. By randomized trials of at-and sub-wavelength deposited  $\text{VO}_2$  nano/micro-  
28 features, a periodic  $\text{VO}_2$  nanowire array and a solid  $\text{VO}_2$  monolayer that sandwiches a quarter-  
29 wave thick lossless dielectric. Fabricated  $\text{VO}_2$  nanowires typically of 50-150 nm in diameter were  
30 recently used demonstrating the breakdown on the Franz-Wiedemann law in thermoelectricity

31 [25]. These VO<sub>2</sub> nanowires were fabricated through vapor transport method, a bottom-up method  
32 [25-28], and these VO<sub>2</sub> nanobeams can be laid and aligned in-plane, compared to the top-down  
33 photolithography and etching processes for traditional at-wavelength gratings [24]. This bottom-  
34 up method can greatly reduce complexity in fabrication, where minimal coating thickness is  
35 needed.

36 We utilize a Monte-Carlo optimization method to obtain the best nanowire array period and  
37 width of square cross-section VO<sub>2</sub> nanowires [29]. This method is applied to obtain the VO<sub>2</sub>  
38 monolayer as well, which serves as a gradual index anti-reflection layer above the fully-reflecting  
39 silver substrate. The broadband reflectance or broadband emissivity turn-down performance is  
40 quantified with a turn-down performance figure-of-merit (FOM), and compared with other VO<sub>2</sub>  
41 phase transition passive thermal radiation self-cooling coatings. The proposed structure has a total  
42 thickness of about 2.5 μm, including the 500 nm silver substrate. In this design, the coating on a  
43 flexible polymer backing sheet can be applied to alleviate the loss in efficiency for solar cells,  
44 whose temperatures can be as high as 80°C in summers under highly irradiative climates, such as  
45 Texas. The flexible coating can be applied to one or both sides of a vacuum gap between a solar  
46 cell housing and the roof. Similarly, it can be utilized for cooling compact processor components  
47 that gets as warm as 80 to 100°C. Other usages include thermal management for lithium-ion cells  
48 casings, passive-switched spacecraft insulation blankets, and other common Earth-temperature  
49 thermal regulation applications.

## 50 2. COMPUTATIONAL METHODS

### 51 2.1. Theory of Optical Coatings

52 In this paper, Rigorous Coupled-Wave Analysis (RCWA), a well-established multilayered  
53 diffraction method to solve Maxwell equations [30, 31], is utilized to calculate the optical radiative  
54 properties of the optimized periodic coatings. The materials and geometrical parameters of the  
55 proposed coating is shown in Figure 1: The grating has a period of  $\Lambda$ , nanowire width of  $w$ ,  
56 nanowire height of  $h$ , distance between nanowires  $b$ , thickness of the lossless dielectric is  $d_D$ , and  
57 thickness of the VO<sub>2</sub> sub-monolayer is  $d_{VO_2}$ . Initially, the nanowire aspect ratio can be non-square  
58 to demonstrate possible effects.

59 In designing toward desirable high reflection or high emission properties, selection of optical  
60 parameters is important in tailoring its optical parameters. The contrast of the dielectric layers

61 helps construct an anti-reflecting coating, where each transparent layer satisfies the geometric  
62 mean of the surround layers, such that  $n_1 = \sqrt{n_0 n_2}$  [32]. The underlying totally reflecting metal  
63 substrate can vary among aluminum, silver, gold, and others that are opaque and reasonably  
64 produced at sub-micron thickness. The anti-reflecting layer thicknesses must also satisfy quarter-  
65 wave law, such that  $h = \lambda/4n$ . This quarter-wave method is widely used to determine broadband  
66 reflectance at certain wavelength range known as Bragg reflector, where high- and low- refractive  
67 index materials are stacked into multilayers with quarter-wave thickness [33]. On the other hand,  
68 Fabry-Perot resonance are formed by constructive interference of electromagnetic waves within  
69 the dielectric spacer sandwiched by metallic thin films. Ideally, these metallic boundaries are  
70 infinitesimally-thin and lossless. This produces perfect absorptivity or emissivity, and perfect  
71 transmissivity at moded frequencies [8, 9]. The switching between one to the other mechanism is  
72 how our turn-down capability is designed. In addition, for periodic features at the sub-wavelength,  
73 such that  $\Lambda \ll \lambda$ , effective medium theory (EMT) can be applied to approximate the optical  
74 properties of gratings as expressed by a single layer composed of a filling ratio of dielectric  
75 functions [31, 34].

## 76 **2.2. Radiative Properties**

77 The dielectric function of VO<sub>2</sub> are obtained from empirical spectroscopy of its thin films [35].  
78 Its optical properties are expressed with effective medium and Fermi-Dirac like distribution as  
79 shown,

$$80 \quad \varepsilon_{\text{eff}}^{0.3} = (1-f)\varepsilon_i^{0.3} + f\varepsilon_m^{0.3} \quad (1)$$

$$81 \quad f(T) = \frac{1}{1 + \exp\left[\frac{W}{k_B}\left(\frac{1}{T} - \frac{1}{T_h}\right)\right]} \quad (2)$$

82 where  $\varepsilon_i$  and  $\varepsilon_m$  is the dielectric function for insulator and metal VO<sub>2</sub> respectively.  $W=3.37$  K is  
83 width of the temperature range of metal-insulator transition. The partial monoclinic-to-rutile lattice  
84 phase transition occurs at  $T_h = 78.5^\circ\text{C}$ , where at this temperature, 50% of VO<sub>2</sub> is metallic [35].  
85 Thus, the onset transition temperature of VO<sub>2</sub> from insulator to metal is  $68^\circ\text{C}$ . In Fig. 2 (a), the  
86 imaginary part of the refractive index in VO<sub>2</sub> for the cold state is close to zero in the mid- to far-

87 infrared (around 4 to 10  $\mu\text{m}$ ). This infrared transparent region is highlighted in gray, and can play  
 88 an important role in low absorption. On the other hand, it is absorbing in visible and far-infrared  
 89 region.

90 As shown in Fig. 2(b), there are a few broadly infrared-transparent dielectric candidate  
 91 materials that can be utilized as the dielectric spacer. These include barium fluoride ( $\text{BaF}_2$ ), zinc  
 92 sulfide ( $\text{ZnS}$ ), and silicon ( $\text{Si}$ ). The most common, silicon, has broadly constant refractive index  
 93 of around  $n = 3.4$ , with no extinction coefficient provided undoped low number density and optical  
 94 quality [31]. For  $\text{BaF}_2$  and  $\text{ZnS}$ , the refractive index is lower, but have absorption component in  
 95 far infrared region, due to the Reststrahlen effect of gaps in the upper-level electron bands [36, 37]  
 96 The lower refractive index is appreciated in the arrangement of anti-reflection gradient index of  
 97 layers. In certain other turn-down coating designs,  $\text{MgF}_2$  can also be the candidate for the dielectric  
 98 materials. However, it has a significant absorption near the Reststrahlen band, which may result in  
 99 reduction in the performance of radiative properties [38]. Insulators with absorption in infrared  
 100 wavelengths up to 30  $\mu\text{m}$  must be avoided, as a wavelength window cutoff in the upper limit leaves  
 101 more than 10% of Planck radiation at atmospheric temperatures unaccounted for. The balance of  
 102 broad infrared transparency and close to unity refractive index needs to be considered.

### 103 **2.3. Optimization of Parameters**

104 The parameter optimization scheme is conducted by creating four arrays of random  $N$   
 105 numbers,  $r_i$ , for randomizing  $\Lambda$ ,  $b$ ,  $h$ , and  $d_{\text{VO}_2}$ . The arrays consisting of random numbers are then  
 106 used to produce random value of size arrays for those four parameters as:  $\Lambda = \Lambda_0 \pm r_1\Lambda_0$ ,  $b = b_0 \pm$   
 107  $r_2b_0$ ,  $h = h_0 \pm r_3h_0$ , and  $d_{\text{VO}_2} = d_0 \pm r_4d_0$ . Candidates with  $b > \Lambda$  are rejected. The  $N$  combinations  
 108 of candidates are created and evaluated with the following figure-of-merit (FOM),

$$109 \quad \text{FOM} = \frac{R_{300}}{R_{350}} = \frac{\int_{0.3\mu\text{m}}^{30\mu\text{m}} \rho_{\lambda,300} E_{\text{BB},300} d\lambda}{\int_{0.3\mu\text{m}}^{30\mu\text{m}} \rho_{\lambda,350} E_{\text{BB},350} d\lambda} \quad (3)$$

110 where  $\rho_\lambda$  is the spectral reflectivity, and  $E_{\text{BB},T}$  is the spectral emissive power which expressed as  
 111  $E_{\text{BB},T} = \pi I_{\text{BB},T}$ , where  $I_{\text{BB},T} = (4\pi^2 c_0^2 \hbar / \lambda^5) / [\exp(2\pi \hbar c_0 / \lambda k_B T) - 1]$  is the blackbody intensity at  
 112 the corresponding temperature  $T$ . The integrated wavelength ranges from 0.3  $\mu\text{m}$  and 30  $\mu\text{m}$ , which  
 113 covers adequate sampling of the blackbody spectrum at atmospheric temperatures up to the Solar

114 spectrum. The FOM is based on coating reflectivity to normalize from the opaque metal substrate,  
115 for sake of FOM comparison with other configurations on other metal substrates. The reflectivity  
116 is used to assess the coating's ability to reject surrounding radiation at higher temperature. On the  
117 other hand, for other calculations, the spectral emissivity is calculated as  $\epsilon_\lambda = 1 - \rho_\lambda$ , considering  
118 that Kirchhoff's law of radiation is satisfied being the substrate is thick enough to be opaque. By  
119 fitting the parameter inputs into this summative FOM metric, further parametric stipulations can  
120 be applied to the next round of optimizations as explained in next section. Since the optimization  
121 consists of four parameters to randomize,  $N = 10^4$  candidates are sufficient to search for the optimal  
122 structure. Yet optimizing more parameters could require additional samples needed, but recent  
123 machine learning techniques such as Bayesian optimization may be implemented in the future for  
124 its adaptive learning of the best parameters with reasonable convergence [39].

### 125 3. RESULTS AND DISCUSSION

#### 126 *3.1. Radiative Turn-Down Performance of Optimized Coating*

127 In this work, BaF<sub>2</sub> is chosen as the dielectric spacer and  $d_{\text{BaF}_2}$  is quarter-wave thickness set  
128 constant as  $\lambda_0 / 4n_{\text{BaF}_2} = 1.385 \mu\text{m}$ . The center wavelength  $\lambda_0$  is chosen as  $8.2 \mu\text{m}$ , corresponding  
129 to emissive power at  $80^\circ\text{C}$  (hot condition). The cold condition is selected to be  $30^\circ\text{C}$ , a typical  
130 warm day or summer night in Texas. BaF<sub>2</sub> has a low index of approximately  $n_{\text{BaF}_2} = 1.5$ , which  
131 contrasts highly against VO<sub>2</sub>. BaF<sub>2</sub> is preliminarily selected as the lossless dielectric due to its  
132 broad essentially zero imaginary component of the refractive index up to the Reststrahlen  
133 absorption peak near  $50 \mu\text{m}$  [36]. The dielectric function of Ag is Drude-like with plasma constants  
134 from Ref. [1], and that of BaF<sub>2</sub> is obtained from Ref. [37].

135 First, the  $d_{\text{VO}_2}$  sub-monolayer is found to have optimal thickness at  $450 \text{ nm}$  via our  
136 randomization trials. It is thinner than the anticipated quarter-wave thickness of  $\lambda_0 / 4n_{\text{VO}_2} = 840$   
137 nm, where  $n_{\text{VO}_2} = 2.38$  at  $\lambda = 8.2 \mu\text{m}$ . The maximized FOM is quite broad over  $N = 10^4$  samples,  
138 with no random scattering of outliers. Deviations of a few tens of nanometers from this value  
139 remains high performance. On searching for an optimal filling ratio of VO<sub>2</sub> nanowire-to-period ( $\phi$   
140  $= w / \Lambda$ ), we narrowed it to the range between 0.4 to 0.6. Thus, a reasonable additional restriction  
141 can be applied to the optimization method where the width of the VO<sub>2</sub> nanowire cross-section is  
142 equal to the nanowire height. Optimizations of rectangular nanowires did not result in additional

143 maximization of FOM. Square cross-section VO<sub>2</sub> nanowires with high length-to-width aspect  
 144 ratios have been realized for nanoscale applications [23]. This round of optimizations is conducted  
 145 with the aspect ratio restrictions, resulting in the best optimized structure with parameters:  $\Lambda =$   
 146 194 nm,  $b = 114$  nm,  $w = h = 80$  nm,  $d_{\text{BaF}_2} = 1.385$   $\mu\text{m}$ , and  $d_{\text{VO}_2} = 0.450$   $\mu\text{m}$ . This design  
 147 corresponds to the highest FOM = 1.47, meaning that the emitted thermal radiation at high  
 148 temperature exceeds that absorbed at low temperature.

149 The thermal radiation turn-down mechanism can be explained starting with Fig. 2(a), where  
 150 the large difference of extinction coefficient  $\kappa$  between 30°C and 80°C is observed in the  
 151 highlighted gray region of the spectrum. This component is close to zero at the low temperature,  
 152 but well above one and increasing in magnitude in the mid to far infrared region at the high  
 153 temperature. Figure 3(a) shows the averaged spectral emissivity between TM- and TE-polarized  
 154 waves calculated by RCWA. The emissivity is unavoidably high at any temperature in the visible  
 155 wavelengths, as there is always a bandgap transition. Meanwhile in the infrared region, the region  
 156 corresponding to the extinction coefficient flip overlaps with the atmospheric transparency  
 157 window (inverse of clouds on a warm day near 290 K). With the optimized design, the emissivity  
 158 switches between low emissivity and high emissivity as the temperature increases. Additionally,  
 159 the hemispherical emissivity ( $\epsilon^{\text{h}}$ ) across all polar incident angles and averaged electromagnetic  
 160 wave polarizations shows small differences compared to the normal emissivity, except for the far-  
 161 infrared region beyond 25  $\mu\text{m}$ . This is attributed to some minor absorption due to the off-quarter-  
 162 wave thickness attenuation length from a slightly lossy BaF<sub>2</sub> as it approaches its Reststrahlen band,  
 163 and will be dissected in our forthcoming discussion.

164 The normal polar incident angle emissivity in transverse magnetic (TM) and transverse electric  
 165 (TE) wave calculated in effective medium theory (EMT) are shown in Fig. 3(b), and it shows  
 166 drastic differences between them. This is due to differences in effective refractive index in  
 167 extraordinary and ordinary components, as expressed by [34],

$$168 \quad \epsilon_{\text{TM}} = \frac{\epsilon_{\text{VO}_2} \epsilon_{\text{air}}}{(1 - \phi) \epsilon_{\text{VO}_2} + \phi \epsilon_{\text{air}}} \quad (4)$$

$$169 \quad \epsilon_{\text{TE}} = \phi \epsilon_{\text{VO}_2} + (1 - \phi) \epsilon_{\text{air}} \quad (5)$$



170 where  $\phi$  is the width-to-period filling ratio for gratings. The index of air is  $\epsilon_{\text{air}} = 1.0$ . The resulting  
 171 effective refractive index for TM wave is calculated at around  $n_{\text{TM}} \sim 1.3$ , and has low  $\kappa_{\text{TM}}$  value for  
 172 both 30°C and 80°C, which suppresses the emissivity. On the other hand, the contribution of VO<sub>2</sub>  
 173 is much higher in the effective refractive index for TE waves, which  $n_{\text{TE}} \sim 1.7$  and  $\sim 3.6$  at 30°C  
 174 and 80°C, respectively. The  $\kappa_{\text{TE}}$  value is much higher at 80°C, given by 2.0 to 4.0, and so higher  
 175 emissivity is obtained. We note the near-perfect emissivity of 0.997 at 10.5  $\mu\text{m}$ , attributed to the  
 176 optimized design of the Fabry-Perot mechanism.

177 The following figures further investigate the underlying mechanisms of the turn-down  
 178 coating's near-idealized performance. Figure 4 shows the emissivity calculated by RCWA as a  
 179 function of both incident angle and wavelength. The results show the high turn-down performance  
 180 of emissivity between cold and hot cases for both TM and TE waves. This is especially true in the  
 181 neighborhood of 10  $\mu\text{m}$ , as the normal and broadly oblique emissivity switches from near-zero to  
 182 near-unity. The emissivity in the TM wave is slightly suppressed due to the extinction coefficient  
 183 in the effective medium extraordinary polarization being close to zero for higher temperature. On  
 184 the other hand, the contrast in TE wave polarization is higher due to the switch between insulating  
 185 and metallic dispersion along the nanowire. In essence, the axial dispersion along the nanowire  
 186 offers the highest contrast corresponding to the TE polarization, while maintaining good  
 187 transmittance overall due to the sparsity of interactions of electric fields along the nanowire cross-  
 188 section. Interestingly, the high emissivity observed at far-infrared region for TM wave is not  
 189 present at TE wave. EMT was also able to capture the angular polarization dependency in TM  
 190 wave, where the emissive power is produced only in  $x$ - $z$  plane at normal polar incident angle.

191 Figure 5 demonstrates the power dissipation density (PDD) plots between cold and hot states.  
 192 PDD in  $\text{W}/\text{m}^3$  is given by,

$$193 \quad \text{PDD} = \frac{1}{2} \epsilon_0 \text{Im}(\epsilon) \omega |\mathbf{E}|^2 \quad (6)$$

194 where  $\omega$  is the angular frequency corresponding to the wavelength, and  $\mathbf{E}$  is the local electric field  
 195 as function of the  $x$ - $z$  plane. In Fig. 5 (a), the mechanism behind the high reflectance in the cold  
 196 state is due to graded refractive index from top to bottom. With  $\phi = 0.4$ , the effective refractive  
 197 index of the nanowires is  $n_{\text{EMT}} = 1.55$ , close to the refractive index of the dielectric,  $n_{\text{BaF}_2} = 1.44$

198 at 30°C and 8  $\mu\text{m}$  wavelength. As the nanowire width becomes infinitesimally small the FOM  
199 plateaus close to 1.5. This makes sense as the VO<sub>2</sub> layer seeks to obtain a refractive index close to  
200 unity. The spectra calculated with an 80 nm-thick effective nanowire medium resulted the same  
201 normal emissivity, with discernable differences of off-normal spectra due to the anisotropic  
202 effective medium distribution [34]. The refractive index of the sub-monolayer VO<sub>2</sub> is  $n_{\text{VO}_2} = 2.38$ ,  
203 which is a gradual transition to higher index before the reflecting and opaque silver substrate. The  
204 power is concentrated in a sliver at the interface between the VO<sub>2</sub> sub-monolayer and silver. Using  
205 the penetration depth definition  $\delta = \lambda / 4\pi\kappa$ , the attenuation depth in the silver substrate is 11 nm,  
206 almost negligible. Some absorption is seen in VO<sub>2</sub>, and none through the BaF<sub>2</sub> dielectric cavity  
207 layer, as the fields are transmitted in the cold state. Since the extinction coefficient of VO<sub>2</sub> is non-  
208 zero ( $\kappa = 0.08$  at 8  $\mu\text{m}$ ) in the transparency region shown in Fig. 2(a), the reflection is not perfect.  
209 This 5.7% VO<sub>2</sub> monolayer thickness to its penetration depth ratio is expressed correspondingly in  
210 the minimum emissivity at 8  $\mu\text{m}$  shown in Fig. 3(a).

211 On the other hand, from Fig. 5 (b), the electromagnetic field power dissipation density (PDD)  
212 within the VO<sub>2</sub> nanowire and VO<sub>2</sub> bottom layer at the hot state temperature shows higher  
213 absorption compared to lower temperature due to its much higher  $\kappa$  value of 3.3. In the hot state,  
214 the 450 nm-thick VO<sub>2</sub> sub-monolayer becomes to the metallic substrate, such that the lossless  
215 dielectric insulator becomes a Fabry-Perot resonator. This plasmonic resonance is induced within  
216 the nanowire and within the BaF<sub>2</sub> layer due to its metallic phase in vanadium dioxide layer,  
217 behaving like metal-insulator-metal (MIM) [40]. Localization of power absorption can be up to  
218 1000 W/m<sup>3</sup> in both VO<sub>2</sub> layers. The finesse in this optimized design is due to the upper metal layer  
219 being a loosely-packed thin metal film, such that enough radiation is able to enter the dielectric  
220 cavity and constructively interfere to induce maximum absorption. Hence, the adaptive design  
221 switches from anti-reflecting coating by refractive index gradient layering to a plasmonic resonant  
222 cavity that concentrates power absorption/emission within the VO<sub>2</sub> during the coating's hot state.

223 Although many optical materials and coatings should perform well regardless of radiation  
224 incident angle, some angular dependence is observed at far infrared region at around 28  $\mu\text{m}$ . In  
225 Figure 6, we investigate the anomalous high absorption marked by the TM wave "lobes" in Fig. 4  
226 (a) and (b). The absorptive effect is due to a thick BaF<sub>2</sub> layer, where spectral emissivity increases  
227 with incident angle and reaches up to 1.0 at higher angles due to increasing value of  $\kappa$  value and

228 propagation length. Neither the silver substrate nor the VO<sub>2</sub> components have effects on the  
229 oblique angle emissivity. The incident far infrared light is trapped in the slightly lossy cavity and  
230 constructs multiple reflections between VO<sub>2</sub> NW and VO<sub>2</sub> sublayer. This phenomenon is only  
231 observed in TM waves at oblique incident angles, as the electric fields form surface plasmon modes  
232 at the lower corners of the dielectric VO<sub>2</sub> nanowires [41] The emissivity is further enhanced at hot  
233 state (Figs. 6 d-f) because metallic phase in VO<sub>2</sub> absorbs the light, especially the under-cavity  
234 monolayer. At steeper angles, emissive power is then concentrated within BaF<sub>2</sub> cavity, as the  
235 mechanism transitions toward cavity extinction and trapping. In practice, this angle-dependent  
236 emissivity in cold state should be avoided to improve its overall performance with radiation  
237 coming from any polarization type. With this consideration of the Reststrahlen band extinction of  
238 this particular infrared material, other dielectric materials should be considered as replacement, as  
239 discussed in the next section.

### 240 **3.2. Performance Enhancement by Dielectric Spacer Types**

241 Figure 7 (a) shows a sweeping of a correspondingly quarter-wave thick layer of purely real  
242 component and wavelength-independent refractive indices from unity to Germanium ( $n = 4.0$ ).  
243 The VO<sub>2</sub> parameters are unchanged from the previously-found optimized configuration. Here, a  
244 higher FOM performance was found by an idealized dielectric spacer of refractive index  $n = 2.2$ .  
245 This FOM can be as high as 1.86, slightly higher compared to the optimized structure with BaF<sub>2</sub>  
246 of 1.47. In this regard, we learn that other broadly infrared-transparent materials with higher index  
247 such as silicon ( $n = 3.4$ ) could achieve similar turn-down performance. Other low-index materials  
248 can have similar FOM as the BaF<sub>2</sub> configuration, such as potassium chloride ( $n = 1.49$ ) and  
249 potassium bromide ( $n = 1.55$ ), as long as the Reststrahlen band is far beyond the thermal infrared  
250 regime ( $\lambda > 40 \mu\text{m}$ ). Ideally, medium-index materials such as zinc selenide ( $n = 2.4$ ) or zinc sulfide  
251 ( $n = 2.2$ ) can deliver FOM  $> 1.47$ . It becomes pressing to seek crystalline and interfacial  
252 compatibility between these medium-index dielectrics with VO<sub>2</sub>. Difficulties may arise in more  
253 common dielectric oxides with medium-index, such as silicon dioxide or titanium dioxide, due to  
254 their Lorentz absorption in the mid- to far-infrared [42].

255 In the next investigation shown in Fig. 7 (b), it was found the filling ratio of the VO<sub>2</sub> NW array  
256 plays an important role in high reflectance in cold state due to index-matching between the VO<sub>2</sub>  
257 NW / air effective medium (EMT) layer and the dielectric material. The previous investigation for

258 BaF<sub>2</sub> shows it reached a maximum at  $\phi = 0.4$ , but it is not true for the other dielectric materials.  
259 The highest FOM is achieved for both ZnS and the constant  $n = 2.2$  index at  $\phi = 0.3$ . The slightly  
260 lower FOM of ZnS compared to constant  $n = 2.2$  is due to its closer Reststrahlen band peak at 30.5  
261  $\mu\text{m}$  [37]. For a high-index dielectric such as Si, the best filling ratio of the VO<sub>2</sub> NW array is zero,  
262 which is unrealistic. This is due to the departure of index-gradient matching. For instance, the  
263 effective refractive index within the visible to near infrared region of EMT is  $n_{\text{EMT}} = 1.0\sim 2.0$  for  
264 filling ratio of  $\phi = 0.4$ , which matches overall with the refractive index of the BaF<sub>2</sub> cavity,  $n_{\text{BaF}_2} =$   
265 1.4~1.5. Other dielectric materials such as zinc sulfide (ZnS) and silicon (Si) may replace BaF<sub>2</sub>  
266 with an appropriate filling ratio to improve overall reflectance, but with consideration of realizable  
267 nanowire sizing. Other dielectric spacers have been used in other studies of turn-down coatings,  
268 which we will make a comparison.

### 269 **3.3 Comparison of Radiative Turn-Down Performance**

270 Figures 8 (a) and (b) compares the reflectance at cold state and the emissivity at the hot state  
271 of our optimized structure (VO<sub>2</sub> nanowires / BaF<sub>2</sub> / VO<sub>2</sub>) with a rudimentary quarter-wave (QW)  
272 layers as first-order approximation (BaF<sub>2</sub> QW / VO<sub>2</sub> QW), a Fabry-Perot resonator (thin VO<sub>2</sub> / Si)  
273 [9], and a multi-component radiative cooler system (Multilayer band-pass filter / VO<sub>2</sub> / MgF<sub>2</sub>)  
274 [15]. The QW layers are presented to demonstrate its comparable high coating transmissivity as a  
275 proof of an anti-reflecting film, similar to our optimized nanowire structure in the cold state. The  
276 Planck emissive power spectrum at 80°C is also posed to predict the total emissivity between the  
277 different configurations. Table I compares the summative radiative performances. The FOM of the  
278 optimized structure is 1.47, higher than other realized structures of 0.86 and 0.6, respectively. The  
279 basic quarter-wave layers that share the same material composition as our optimized structure has  
280 a higher FOM of 1.06. The absence of the semi-metallic upper nanowire array layer produces no  
281 cavity mode interference, but shares a peak local emissivity near 8  $\mu\text{m}$ . The key understanding is  
282 the absence of the upper solid VO<sub>2</sub> layer for the purpose of creating a Fabry-Perot cavity in turn  
283 reduces performance, especially the needed high reflectance in the cold state.

284 Thus, the VO<sub>2</sub> nanowire array is a good compromise in gaining the high turn-down, while any  
285 Fabry-Perot multilayer configuration has lower turn-down performance due to narrower band  
286 emission. We noticed some consequential differences in performance in the multi-component  
287 Fabry-Perot cooler system from our recalculations is likely due to absorption by MgF<sub>2</sub> near its

288 Reststrahlen band near 20  $\mu\text{m}$  [38], as well as differences from more modern spectroscopic surveys  
 289 of VO<sub>2</sub> thin films [35, 43]. Additionally, Table 1 compares the quantities of radiative heat emitted  
 290 to the surroundings. The emitted power at normal incidence is given by,

$$291 \quad E_{\text{emit}} = \int_{0.3\mu\text{m}}^{30\mu\text{m}} \varepsilon_{\lambda,T} E_{\text{BB},T} d\lambda \quad (7)$$

292 where this quantity represents the potential to emit to a neighboring reradiating surface, such as a  
 293 multilayer insulation blanket [44]. The error to these figures is no more than 10% due to the upper  
 294 wavelength cutoff at room temperature and above. We also calculate the integrated hemispherical  
 295 emissivity combined with absorption from atmospheric radiation, given by,

$$296 \quad q''_{\text{net}} = \int_{0.3\mu\text{m}}^{30\mu\text{m}} \varepsilon_{\lambda,T}^{\text{h}} E_{\text{b},T} d\lambda - \int_{0.3\mu\text{m}}^{30\mu\text{m}} (1 - \tau_{\text{atm},\lambda}) \varepsilon_{\lambda,T}^{\text{h}} E_{\text{BB},T_{\text{amb}}} d\lambda \quad (8)$$

297 where  $\tau_{\text{atm},\lambda}$  is the atmospheric transparency shown in Fig. 2(b) [45]. The ambient temperature  $T_{\text{amb}}$   
 298 is assumed to be 290 K. The purpose of presenting this combined net radiative flux is to assess the  
 299 respective coatings' performance exposed to diffuse cloudy or night sky. By analyzing Eq. (7), our  
 300 optimized structure produces 560 W/m<sup>2</sup> in the hot state, while just 53 W/m<sup>2</sup> in the cold state. This  
 301 ratio of power turn-down is 10.6:1. An even higher turn-down ratio is seen with Eq. (8), for net  
 302 hemispherical heat flux with atmosphere, where the ratio is 14.7:1. The magnitudes of the hot state  
 303 emissive power is not insignificant compared to the irradiative power flux from the Sun (~1400  
 304 W/m<sup>2</sup>). The net radiative performance of comparable structures also show good turn-down but at  
 305 predicted lower hot state magnitudes.

306 Although the emissive power turn-down ratio for the simpler QW layers is higher (14.3:1), the  
 307 maximum emitted power is lower, therefore the reduced FOM. This FOM accounts for both the  
 308 turn-down ratio as well as the emissive power difference between hot and cold state. A higher  
 309 magnitude emissive power at the hot state is therefore more important, especially for compact  
 310 components with small radiating surface areas. The optimized VO<sub>2</sub> NW design can also provide  
 311 dense thermal radiative energy directed toward the atmosphere, almost doubling the capability for  
 312 radiative rejection compared to other designs. Furthermore, we learn that the basic quarter-wave  
 313 structure in fact outperforms a Fabry-Perot solid VO<sub>2</sub> layer on dielectric. This means the concept  
 314 of a Fabry-Perot structure may not be best suited, compared to a simpler dual anti-reflection layer.  
 315 We note the performance is bolstered by absorption within the dielectric medium at off-normal  
 316 incident angles. At these emissive power magnitudes at high temperature, these coatings may be

317 capable of passive radiative cooling under the Sun via careful tuning of spectral response in the  
318 visible wavelength.

### 319 **3.4. Evaluation of Daytime Radiative Cooling**

320 This section assesses the possibility of the optimized coating as a daytime radiative cooler, and  
321 the metrics developed to quantify this capability. The Daytime Cooling Merit (DCM) is defined in  
322 Eq. (9),

$$323 \quad \text{DCM} = \frac{P_{\text{cool},350}}{P_{\text{cool},300}} = \frac{P_{\text{coat},350} - P_{\text{atm},350} - P_{\text{sun},350} + P_{\text{con},350}}{P_{\text{coat},300} - P_{\text{atm},300} - P_{\text{sun},300} + P_{\text{con},300}} \quad (9)$$

324 as a ratio of energy balances from the diffuse coating (coat), atmosphere (atm), the Sun (sun), and  
325 combined conduction and convective cooling (con) to an ambient temperature in atmosphere  $T_{\text{amb}}$   
326  $= 290$  K. The coating radiative power flux in  $\text{W}/\text{m}^2$  is obtained by hemispherical integration of the  
327 spectral directional emissivity with blackbody temperature function of the coating. The incoming  
328 atmospheric power flux is calculated with the diffuse atmospheric transparency spectrum seen in  
329 Fig. 3(a), and integrated with the spectral directional absorptivity at ambient temperature. We  
330 obtained the solar absorption spectrum from  $I_{\text{AMI},5,\lambda}$  at normal incidence spectral absorptivity, as  
331 the coating can be mechanically dialed to be sun-pointing. Lastly, heat rejection due to both  
332 convection and conduction to ambient is appropriately grouped into an overall coefficient  $h_c$ ,  
333 which is conservatively set as  $10 \text{ W}/\text{m}^2 \cdot \text{K}$ . The combined power from this component is  $P_{\text{con},T} =$   
334  $h_c \cdot (T - T_{\text{amb}})$ . We note that the integration cutoff for solar irradiation at the lower wavelength of  
335  $0.3 \mu\text{m}$  gives 3% error, compared to the 9% error for the  $30 \mu\text{m}$  upper limit in bodies at terrestrial  
336 temperatures.

337 Applying Eq. (9) onto the optimized structure results in  $\text{DCM} = P_{\text{cool},350} / P_{\text{cool},300} = 271 / (-$   
338  $615) = -0.44$ . This negative DCM indicates that the coating absorbs more sunlight rather than emit  
339 heat at the low temperature near ambient. However, at the high temperature which  $\text{VO}_2$  becomes  
340 metallic, the coating rejects more heat than it absorbs. Since its absorptivity in the visible to near  
341 infrared region is high for any temperature as shown in Fig. 3, the coating's outgoing emissive  
342 power,  $P_{\text{coat},T}$  must overcome the sunlight absorption power,  $P_{\text{sun},T}$ . In Figure 9, plotting the total  
343 radiative outgoing power with temperatures from ambient to  $370$  K, an equilibrium temperature is  
344 reached at around  $T = 345$  K ( $P_{\text{cool},T} = 0$ ) which is just above the phase transition temperature of

345 vanadium dioxide at 340 K. The radiative cooling power drastically increases after passing the  
346 VO<sub>2</sub> phase transition temperature, and it can attain powers up to 470 W/m<sup>2</sup>. This is similar to the  
347 net radiative cooling power at hot state in Table 1. The performance somewhat leans on the  
348 contribution of combined convection and conduction cooling power, in which a well-insulated  
349 environment around the coating may mean less cooling capability at the hot state. Therefore, the  
350 coating is able to reach self-equilibrium near the phase transition temperature of VO<sub>2</sub>. In the  
351 insulating phase near ambient temperature, the coating warms up, but in the metallic phase at high  
352 temperatures, it passively cools.

353 This cooling capability only in the hot state exceeds that of previously designed daytime  
354 radiative cooling coatings, such as SiO<sub>2</sub> / HfO<sub>2</sub> multilayer [46], SiO<sub>2</sub>-polymer hybrid metamaterial  
355 [47], and plain PDMS coatings [48]. Table 2 shows that daytime equilibrium temperature of the  
356 optimized grating is greater than ambient temperature, which does not compare with plain daytime  
357 radiative cooler materials and designs. Rather, the high cooling power just beyond the VO<sub>2</sub>  
358 transition temperature is noticeably significant compared to others. Therefore, we learn that the  
359 optimized VO<sub>2</sub> NW / BaF<sub>2</sub> / VO<sub>2</sub> is useful as a radiative cooler only when in shade and not placed  
360 under the sun. However, it is commendable for this 2 μm-thin coating to ensure that an equilibrium  
361 temperature can be obtained close to 345 K. This is not only helpful in maintaining efficiency in  
362 photovoltaic devices, but also it can be used for thermal management of components such as  
363 rechargeable batteries, fuel tanks, and engines on both terrestrial and space vehicles.

#### 364 4. CONCLUSION

365 We have proposed a self-adaptive high turn-down VO<sub>2</sub> nanowire / BaF<sub>2</sub> / VO<sub>2</sub> / silver thin film  
366 of around 2 μm for passive thermal management applications. Our Monte-Carlo optimization  
367 method was utilized to obtain the optimal structure parameters for VO<sub>2</sub> components. It is compared  
368 with Fabry-Perot multilayers using VO<sub>2</sub>, and a higher figure of merit (FOM) of 1.47 is obtained  
369 compared to other structures (FOM < 1). Ideally, the optimal refractive index of the dielectric  
370 spacer is  $n = 2.2$ , which is slightly higher than BaF<sub>2</sub> ( $n = 1.55$ ). The electric field is reflected at the  
371 interface between VO<sub>2</sub> bottom layer and silver for lower temperature for high reflectance, but a  
372 high value of power dissipation density (PDD) is observed within the VO<sub>2</sub> in higher temperature,  
373 leading to high emissivity in infrared region. The optimized structure provides cooling power of  
374 271 W/m<sup>2</sup> at 350 K whose power is higher compared to previously studies structures. Lastly, this

375 work provides the idea of computational method for optimizing the photonic structures to obtain  
376 the desired optical properties. The obtained data may be utilized for machine learning (ML)  
377 technique to obtain predictive FOM with complex structural geometries and exotic materials, both  
378 dielectrics and phase transition. This structure can be extended to two-dimensional gratings to  
379 possibly further improve its figure-of-merit (FOM) as well as daytime radiative cooling merit  
380 (DCM) turn-down to an even higher value. This turn-down allows the device to self-reject the heat  
381 out of the devices such as solar cells, computer systems, engines, and functions as self-adaptive  
382 radiative cooling device.

383



384 **REFERENCES**

- 385 [1] Zhao, B. and Z.M. Zhang, Study of magnetic polaritons in deep gratings for thermal  
386 emission control. *Journal of Quantitative Spectroscopy and Radiative Transfer*, 135  
387 (2014) 81-89.
- 388 [2] Zhao, B., J.M. Zhao, and Z.M. Zhang, Resonance enhanced absorption in a graphene  
389 monolayer using deep metal gratings. *Journal of the Optical Society of America B*, 32  
390 (2015).
- 391 [3] Araki, K. and R.Z. Zhang, Plasmon-resonance emission tailoring of "origami" graphene-  
392 covered photonic gratings. *Opt Express*, 28 (2020) 22791-22802.
- 393 [4] Chang-Hasnain, C.J. and W. Yang, High-contrast gratings for integrated optoelectronics.  
394 *Advances in Optics and Photonics*, 4 (2012).
- 395 [5] Qiao, P., et al., Theory and design of two-dimensional high-contrast-grating phased  
396 arrays. *Optics Express*, 23 (2015) 24508-24524.
- 397 [6] Qiao, P., W. Yang, and C.J. Chang-Hasnain, Recent advances in high-contrast  
398 metastructures, metasurfaces, and photonic crystals. *Advances in Optics and Photonics*,  
399 10 (2018).
- 400 [7] Harvey, J.E. and R.N. Pfisterer, Understanding diffraction grating behavior: including  
401 conical diffraction and Rayleigh anomalies from transmission gratings. *Optical*  
402 *Engineering*, 58 (2019).
- 403 [8] Wang, L.P., et al., Spatial and temporal coherence of thermal radiation in asymmetric  
404 Fabry–Perot resonance cavities. *International Journal of Heat and Mass Transfer*, 52  
405 (2009) 3024-3031.
- 406 [9] Taylor, S., Y. Yang, and L. Wang, Vanadium dioxide based Fabry-Perot emitter for  
407 dynamic radiative cooling applications. *Journal of Quantitative Spectroscopy and*  
408 *Radiative Transfer*, 197 (2017) 76-83.
- 409 [10] Keçebaş, M.A. and K. Şendur, Enhancing the spectral reflectance of refractory metals by  
410 multilayer optical thin-film coatings. *Journal of the Optical Society of America B*, 35  
411 (2018).
- 412 [11] Uleman, F., et al., Resonant Metagratings for Spectral and Angular Control of Light for  
413 Colored Rooftop Photovoltaics. *ACS Applied Energy Materials*, 3 (2020) 3150-3156.
- 414 [12] Garnett, E.C., et al., Photonics for Photovoltaics: Advances and Opportunities. *ACS*  
415 *Photonics*, 8 (2021) 61-70.
- 416 [13] Li, W., Y. Li, and K.W. Shah, A materials perspective on radiative cooling structures for  
417 buildings. *Solar Energy*, 207 (2020) 247-269.
- 418 [14] Ulpiani, G., et al., On the energy modulation of daytime radiative coolers: A review on  
419 infrared emissivity dynamic switch against overcooling. *Solar Energy*, 209 (2020) 278-  
420 301.
- 421 [15] Ono, M., et al., Self-adaptive radiative cooling based on phase change materials. *Opt*  
422 *Express*, 26 (2018) A777-A787.
- 423 [16] Taylor, S., et al., Spectrally-selective vanadium dioxide based tunable metafilm emitter  
424 for dynamic radiative cooling. *Solar Energy Materials and Solar Cells*, 217 (2020)  
425 110739.
- 426 [17] Torriss, B., J. Margot, and M. Chaker, Metal-Insulator Transition of strained SmNiO<sub>3</sub>  
427 Thin Films: Structural, Electrical and Optical Properties. *Sci Rep*, 7 (2017) 40915.

- 428 [18] Yoo, P. and P. Liao, Metal-to-insulator transition in SmNiO<sub>3</sub> induced by chemical  
429 doping: a first principles study. *Molecular Systems Design & Engineering*, 3 (2018) 264-  
430 274.
- 431 [19] Liu, R., J.-X. Shang, and F.-H. Wang, Electronic, magnetic and optical properties of  $\beta$ -  
432 Ti<sub>3</sub>O<sub>5</sub> and  $\lambda$ -Ti<sub>3</sub>O<sub>5</sub>: A density functional study. *Computational Materials Science*, 81  
433 (2014) 158-162.
- 434 [20] Kort-Kamp, W.J.M., et al., Passive Radiative “Thermostat” Enabled by Phase-Change  
435 Photonic Nanostructures. *ACS Photonics*, 5 (2018) 4554-4560.
- 436 [21] Long, L., et al., Thermally-switchable spectrally-selective infrared metamaterial  
437 absorber/emitter by tuning magnetic polariton with a phase-change VO<sub>2</sub> layer. *Materials*  
438 *Today Energy*, 13 (2019) 214-220.
- 439 [22] Long, L., S. Taylor, and L. Wang, Enhanced Infrared Emission by Thermally Switching  
440 the Excitation of Magnetic Polariton with Scalable Microstructured VO<sub>2</sub> Metasurfaces.  
441 *ACS Photonics*, 7 (2020) 2219-2227.
- 442 [23] Liu, K., et al., Recent progresses on physics and applications of vanadium dioxide.  
443 *Materials Today*, 21 (2018) 875-896.
- 444 [24] Cui, Y., et al., Thermochromic VO<sub>2</sub> for Energy-Efficient Smart Windows. *Joule*, 2  
445 (2018) 1707-1746.
- 446 [25] Lee, S., et al., Anomalously low electronic thermal conductivity in metallic vanadium  
447 dioxide. *Science*, 355 (2017) 371-374.
- 448 [26] Cheng, Y., et al., Structure and Metal-to-Insulator Transition of VO<sub>2</sub> Nanowires Grown  
449 on Sapphire Substrates. *European Journal of Inorganic Chemistry*, 2010 (2010) 4332-  
450 4338.
- 451 [27] Kim, M.W., et al., Substrate-mediated strain effect on the role of thermal heating and  
452 electric field on metal-insulator transition in vanadium dioxide nanobeams. *Sci Rep*, 5  
453 (2015) 10861.
- 454 [28] Shi, R., et al., Low-temperature wafer-scale fabrication of vertical VO<sub>2</sub> nanowire arrays.  
455 *Applied Physics Letters*, 117 (2020).
- 456 [29] Wild, W.J. and H. Buhay, Thin-film multilayer design optimization using a Monte Carlo  
457 approach. *Optics Letters*, 11 (1986) 745-747.
- 458 [30] Moharam, M.G., et al., Formulation for stable and efficient implementation of the  
459 rigorous coupled-wave analysis of binary gratings. *Journal of the Optical Society of*  
460 *America A*, 12 (1995) 1068-1076.
- 461 [31] Zhang, Z.M., *Nano/microscale heat transfer*. 2020.
- 462 [32] Hecht, E., *Optics*. 2017: Pearson Education.
- 463 [33] Inan, H., et al., Photonic crystals: emerging biosensors and their promise for point-of-care  
464 applications. *Chem Soc Rev*, 46 (2017) 366-388.
- 465 [34] Liu, X.L., R.Z. Zhang, and Z.M. Zhang, Near-field radiative heat transfer with doped-  
466 silicon nanostructured metamaterials. *International Journal of Heat and Mass Transfer*, 73  
467 (2014) 389-398.
- 468 [35] Wan, C., et al., On the Optical Properties of Thin-Film Vanadium Dioxide from the  
469 Visible to the Far Infrared. *Annalen der Physik*, 531 (2019) 1900188.
- 470 [36] Andersson, S.K., M.E. Thomas, and C.E. Hoffman, Multiphonon contribution to the  
471 reststrahlen band of BaF<sub>2</sub>. *Infrared Physics & Technology*, 39 (1998) 47-54.
- 472 [37] Querry, M. *Optical constants of minerals and other materials from the millimeter to the*  
473 *ultraviolet*. 1987.

- 474 [38] Giordano, J., Temperature dependence of IR spectra of zinc and magnesium fluoride.  
475 Journal of Physics C: Solid State Physics, 20 (1987) 1547-1562.
- 476 [39] Sakurai, A., et al., Ultranarrow-Band Wavelength-Selective Thermal Emission with  
477 Aperiodic Multilayered Metamaterials Designed by Bayesian Optimization. ACS Central  
478 Science, 5 (2019) 319-326.
- 479 [40] Ogawa, S. and M. Kimata, Metal-Insulator-Metal-Based Plasmonic Metamaterial  
480 Absorbers at Visible and Infrared Wavelengths: A Review. Materials (Basel), 11 (2018).
- 481 [41] Abdulhalim, I., Coupling configurations between extended surface electromagnetic  
482 waves and localized surface plasmons for ultrahigh field enhancement. Nanophotonics, 7  
483 (2018) 1891-1916.
- 484 [42] Kischkat, J., et al., Mid-infrared optical properties of thin films of aluminum oxide,  
485 titanium dioxide, silicon dioxide, aluminum nitride, and silicon nitride. Applied Optics,  
486 51 (2012) 6789-6798.
- 487 [43] Verleur, H.W., A.S. Barker, and C.N. Berglund, Optical Properties of VO<sub>2</sub> between 0.25  
488 and 5 eV. Physical Review, 172 (1968) 788-798.
- 489 [44] Donabedian, M. and D.G. Gilmore, Spacecraft thermal control handbook. 2003:  
490 Aerospace Press.
- 491 [45] Lord, S.D., A new software tool for computing Earth's atmospheric transmission of near-  
492 and far-infrared radiation. Vol. 103957. 1992: Ames Research Center.
- 493 [46] Raman, A.P., et al., Passive radiative cooling below ambient air temperature under direct  
494 sunlight. Nature, 515 (2014) 540-544.
- 495 [47] Zhai, Y., et al., Scalable-manufactured randomized glass-polymer hybrid metamaterial  
496 for daytime radiative cooling. Science, 355 (2017) 1062-1066.
- 497 [48] Mandal, J., et al., Hierarchically porous polymer coatings for highly efficient passive  
498 daytime radiative cooling. Science, 362 (2018) 315-319.

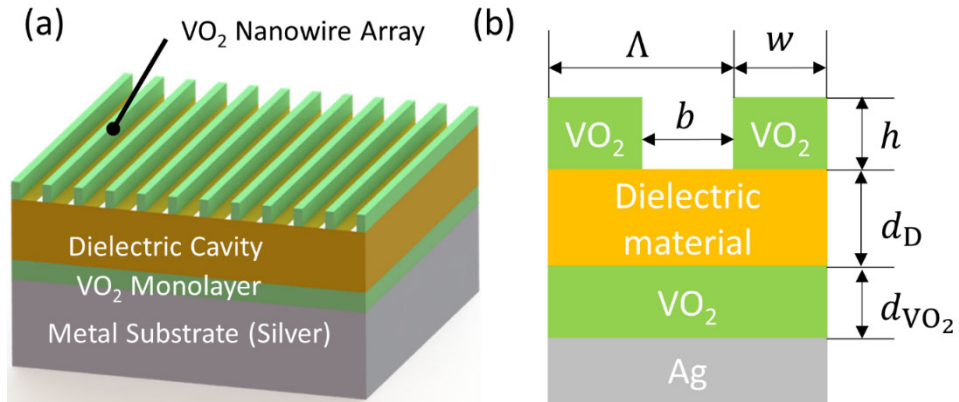


**Fig. 1.** (a) Illustration and schematic of Vanadium Dioxide ( $\text{VO}_2$ ) nanowire / Dielectric material /  $\text{VO}_2$  sub-monolayer coating on Silver (Ag) substrate. (b) Nomenclature of geometric parameters of the coating: Dielectric cavity or monolayer thicknesses  $d$ , nanowire grating period  $\Lambda$ , its width  $w$ , height  $h$ , and groove spacing  $b$ .

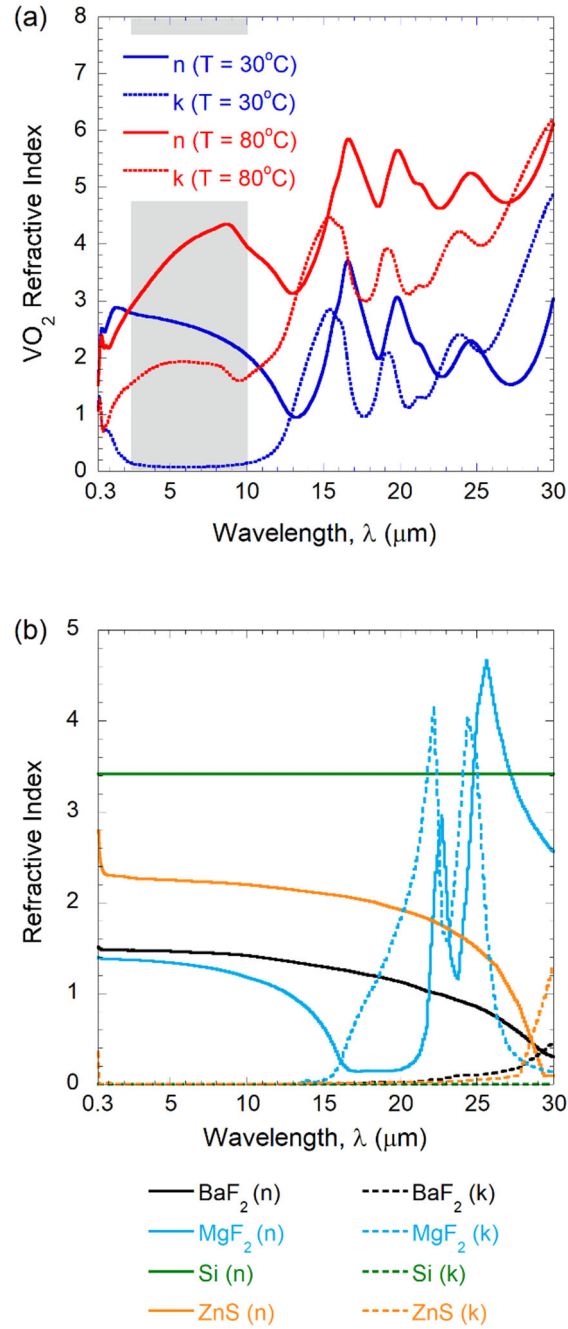


**Fig. 2.** (a) Refractive index of vanadium dioxide (VO<sub>2</sub>) at  $T = 30^\circ\text{C}$  and  $T = 80^\circ\text{C}$  obtained from Ref. [35]. The highlighted region shows near-zero extinction coefficient of the refractive index ( $\kappa$ ) at the cold state. (b) Comparison of refractive index of dielectric materials, including barium fluoride (BaF<sub>2</sub>), magnesium fluoride (MgF<sub>2</sub>), silicon (Si), and zinc sulfide (ZnS).

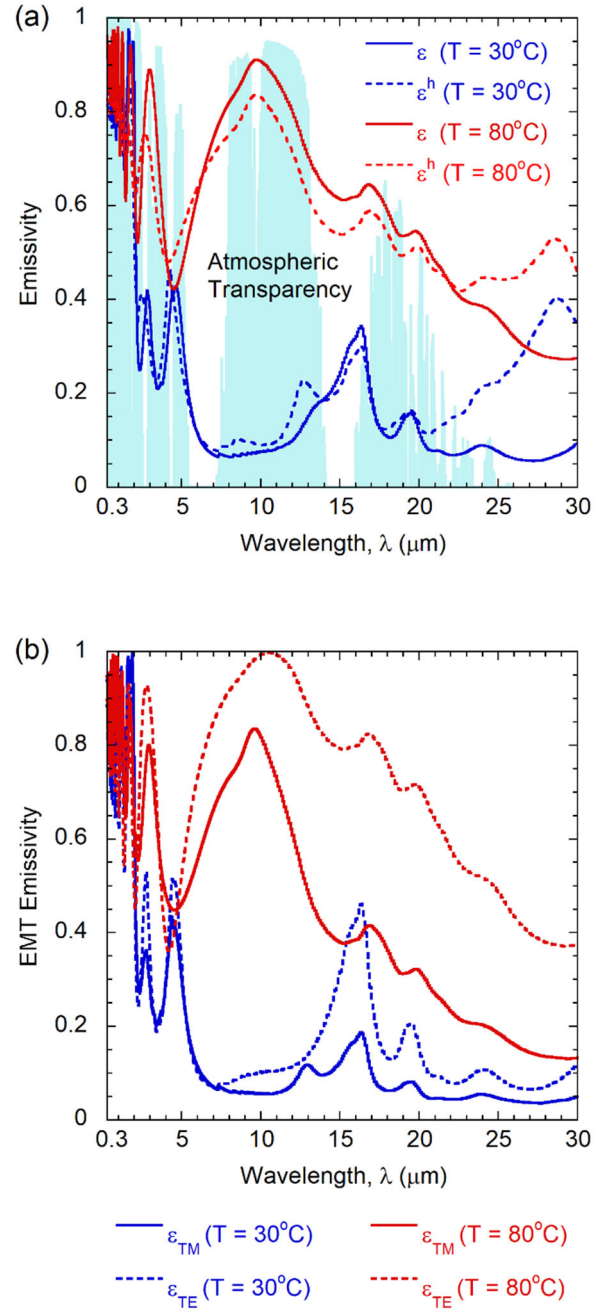


**Fig. 3.** (a) The averaged emissivity spectrum calculated with Rigorous Coupled-Wave Analysis (RCWA). The dashed lines show the hemispherical emissivity spectra. The background atmospheric transparency spectrum is shown in Ref. [45]. (b) Normal emissivity spectrum calculated with Effective Medium Theory (EMT) of optimized VO<sub>2</sub> Nanowire / BaF<sub>2</sub> / VO<sub>2</sub> coating on Ag substrate for TM (solid line) and TE wave (dashed line).

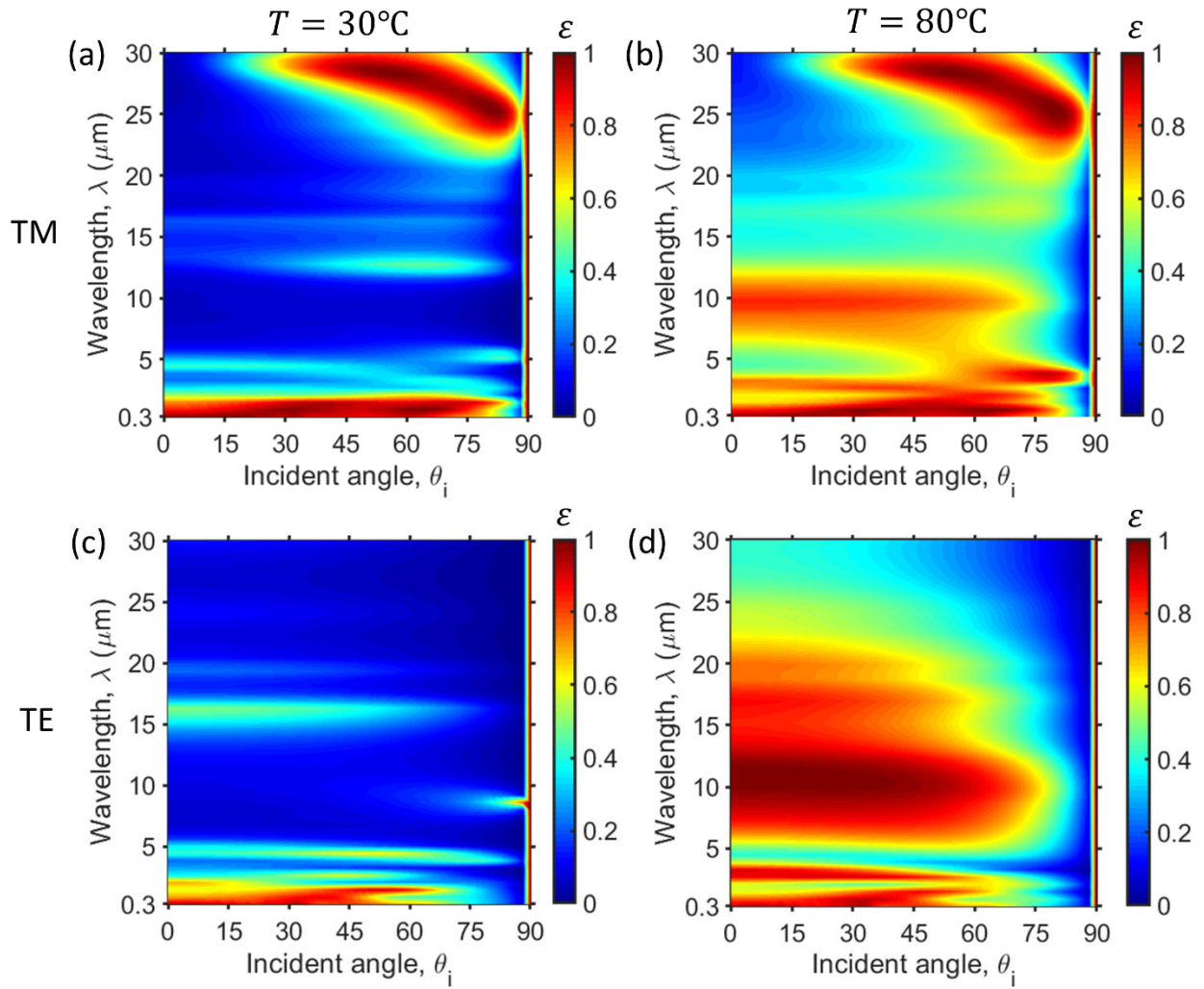


**Fig. 4.** Spectral and incident angle-dependent emissivity contours of TM wave at (a) cold and (b) hot states, and TE wave at (c) cold and (d) hot states, calculated by RCWA.

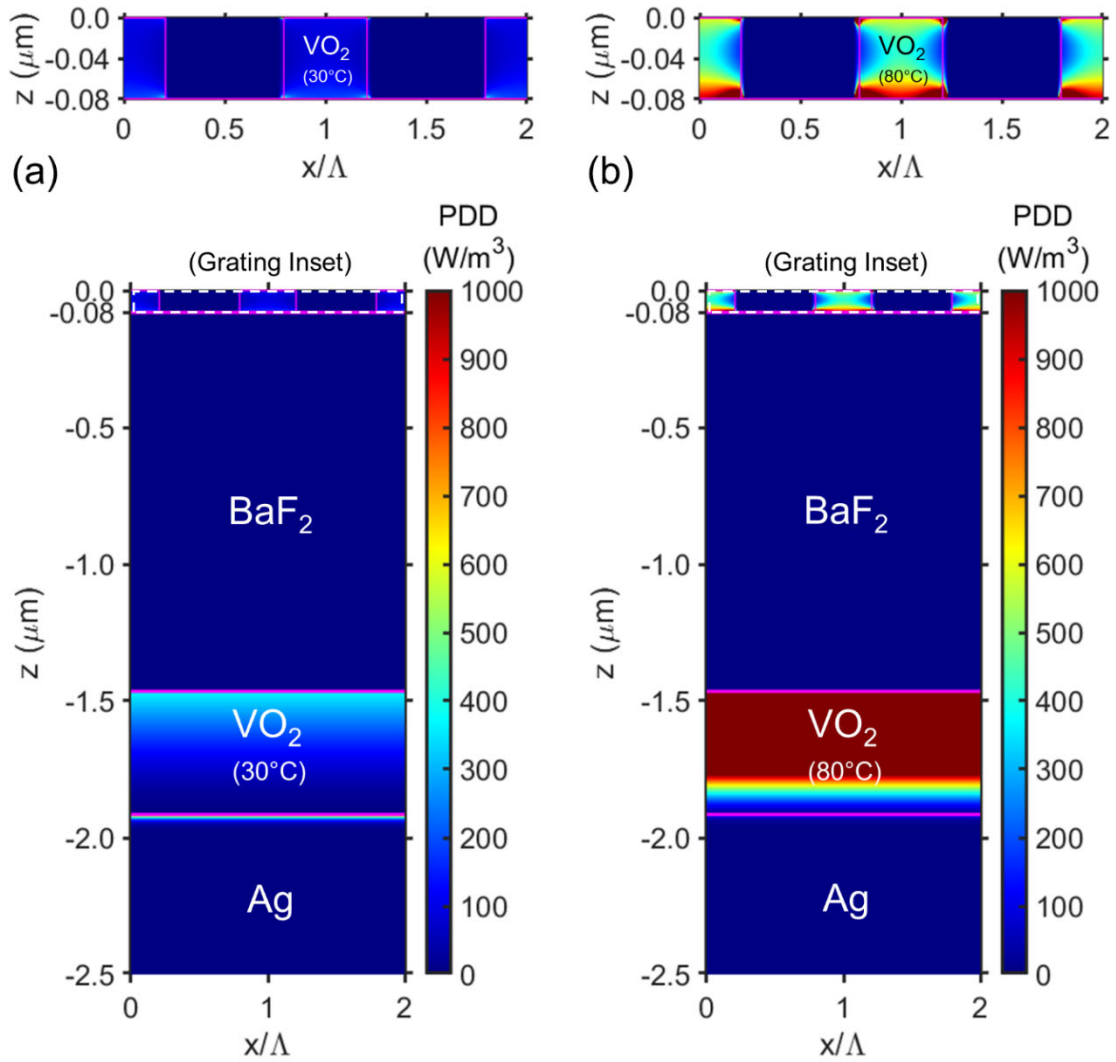


**Fig. 5.** Power dissipation density (PDD) distribution (TM wave only) of the optimized VO<sub>2</sub> NW / BaF<sub>2</sub> / VO<sub>2</sub> design for (a) cold state ( $T = 30^\circ\text{C}$ ) and (b) hot state ( $T = 80^\circ\text{C}$ ) calculated by RCWA. The white dashed box shows the inset figures within the VO<sub>2</sub> nanowire array region. The pink lines delineate the interfaces in the structure.



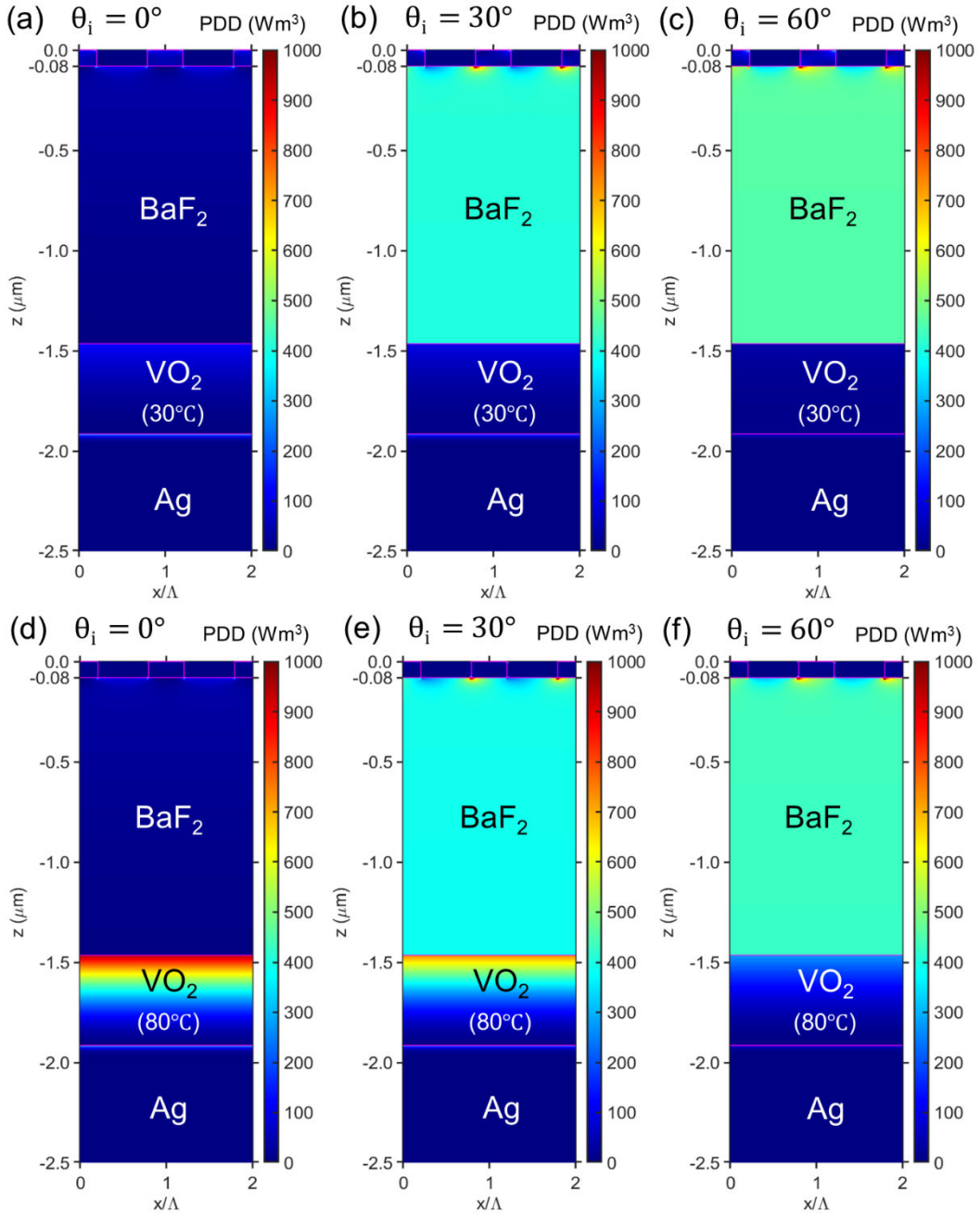


**Fig. 6.** Oblique TM wave power dissipation density (PDD) distribution of the optimized VO<sub>2</sub> NW / BaF<sub>2</sub> / VO<sub>2</sub> design at  $\lambda = 28 \mu\text{m}$  for incident angles: (a)  $\theta = 0^\circ$ , (b)  $\theta = 30^\circ$ , and (c)  $\theta = 60^\circ$  at cold state, and (d)  $\theta = 0^\circ$ , (e)  $\theta = 30^\circ$ , and (f)  $\theta = 60^\circ$  at hot state calculated by RCWA.

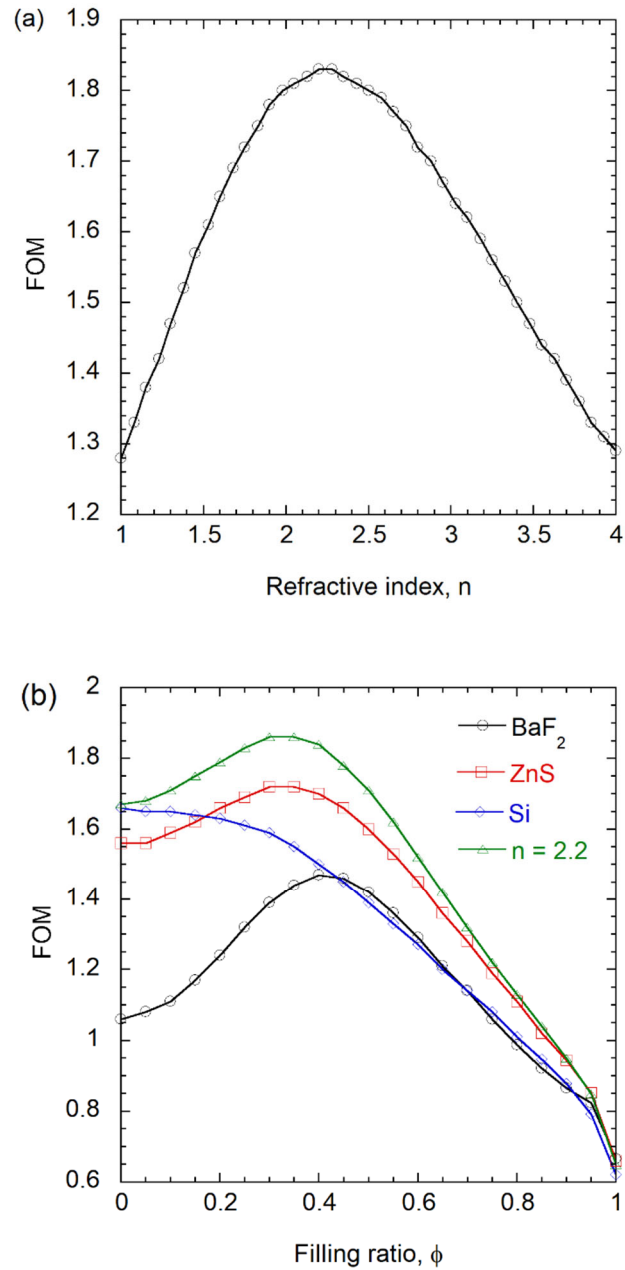


**Fig. 7.** (a) Relationship of FOM and the refractive index of the quarter-wave thick spacer. (b) The correlation of FOM and filling ratio of VO<sub>2</sub> nanowires with different dielectric materials including BaF<sub>2</sub> (black), ZnS (red), Si (blue), and constant  $n = 2.2$  (green).

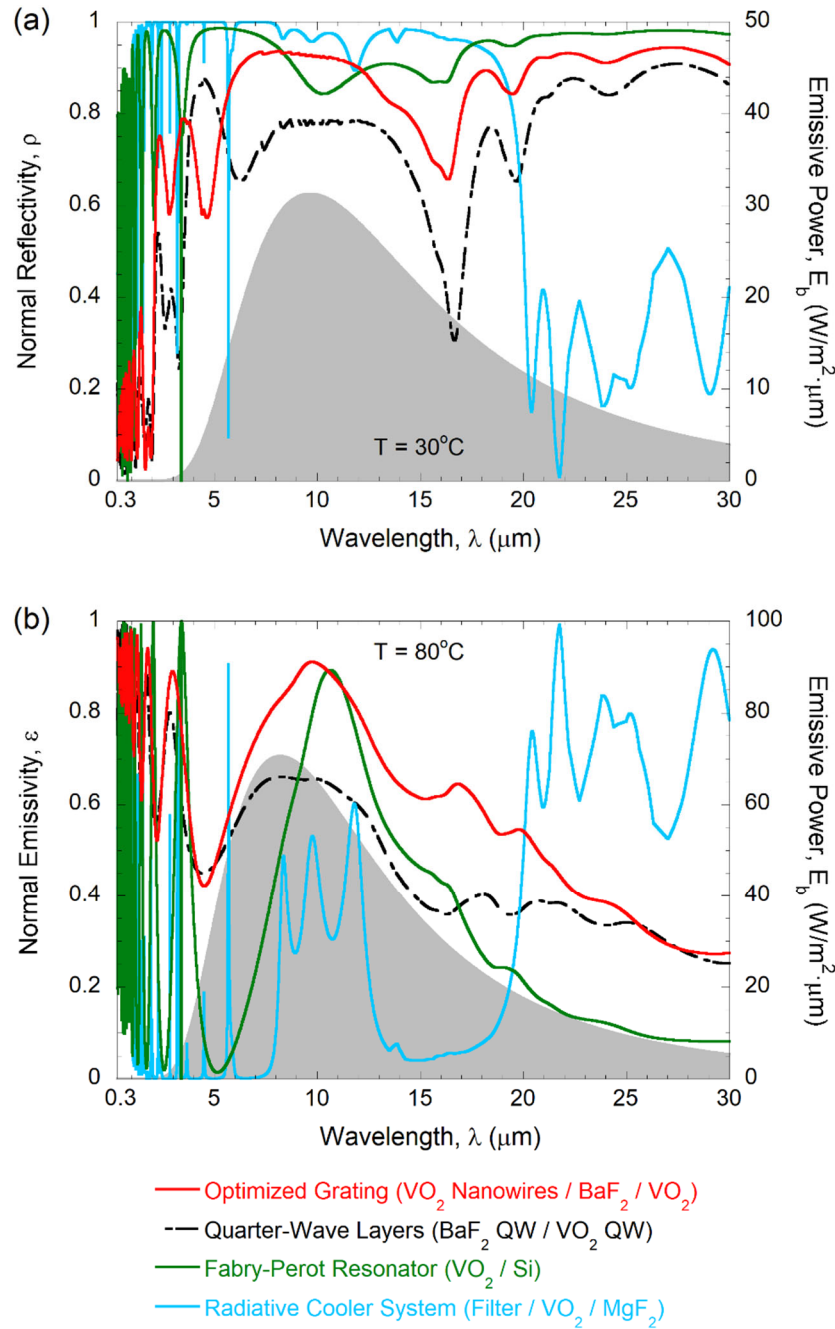


**Fig. 8.** Comparison of (a) normal reflectivity and (b) normal emissivity spectra of this optimized grating ( $\text{VO}_2$  Nanowires /  $\text{BaF}_2$  /  $\text{VO}_2$ ), simple quarter-wave layers ( $\text{BaF}_2$  QW /  $\text{VO}_2$  QW), a Fabry-Perot resonator ( $\text{VO}_2$  / Si), and a radiative cooler system (Band-pass filter /  $\text{VO}_2$  /  $\text{MgF}_2$ ). All are opaque coatings on metal substrates. The Planck blackbody emissive power function ( $E_b$ ) at  $80^\circ\text{C}$  is plotted in shaded gray.

**Table 1.** Comparison of performances among similar turn-down coatings, showing the FOM defined in Eq. (3), the emitted radiation flux ( $\text{W}/\text{m}^2$ ) from the coating ( $E_{\text{emit}}$ ), and the net radiative heat flux between the coating and atmosphere at 290 K ( $q''_{\text{net}}$ ).

Structure	FOM	$E_{\text{emit}}$		$q''_{\text{net}}$	
		30°C	80°C	30°C	80°C
Optimized Grating ( $\text{VO}_2$ Nanowires / $\text{BaF}_2$ / $\text{VO}_2$ )	1.47	53	560	27	396
Quarter-Wave Layers ( $\text{BaF}_2$ QW / $\text{VO}_2$ QW)	1.06	31	443	20	330
Fabry-Perot Resonator ( $\text{VO}_2$ / Si)	0.86	34	359	18	265
Radiative Cooler System (Filter / $\text{VO}_2$ / $\text{MgF}_2$ )	0.60	61	202	17	144

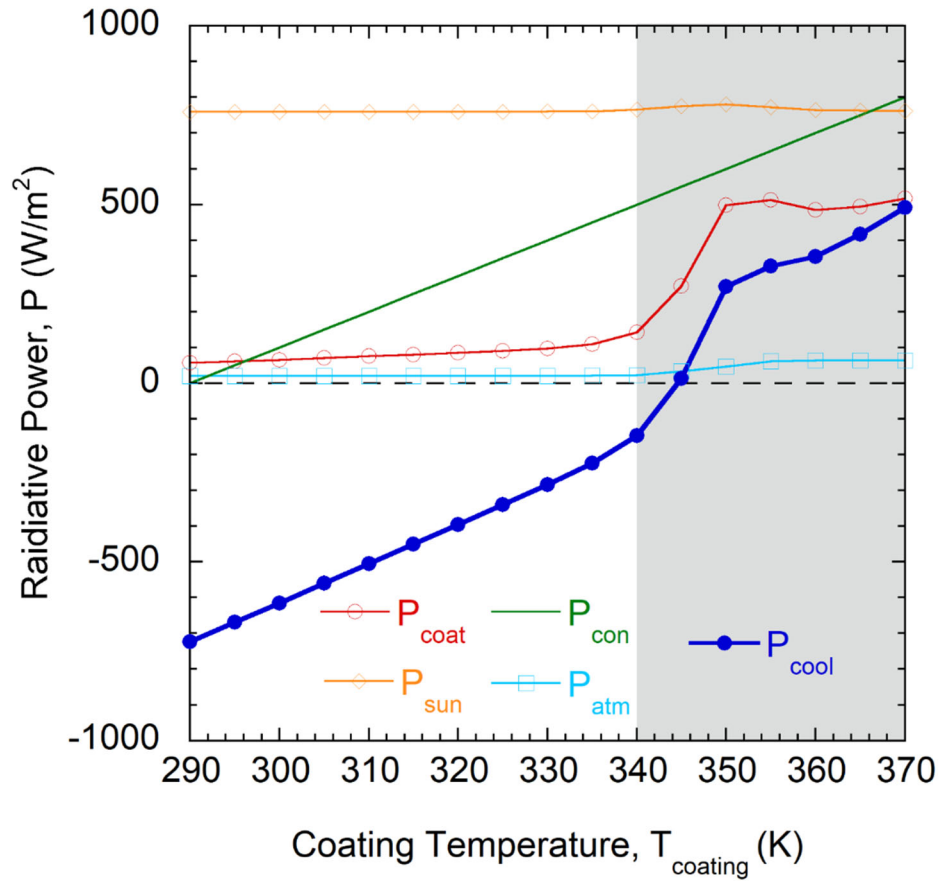


**Fig. 9.** Overall coating radiative cooling power,  $P_{\text{cool}}$  and the temperature of the coating (blue line). The red, light blue, orange, and green solid lines represent  $P_{\text{coat}}$ ,  $P_{\text{atm}}$ ,  $P_{\text{sun}}$ , and  $P_{\text{con}}$ , respectively. The shaded area represents the metallic phase of  $\text{VO}_2$ .

**Table 2.** Comparison of temperature difference  $T_{\text{coating}} - T_{\text{amb}}$  (K), maximum cooling power ( $\text{W}/\text{m}^2$ ), and the Daytime Cooling Merit defined in Eq. (9), with other daytime radiative cooling coatings.

Structure	$T_{\text{coating}} - T_{\text{amb}}$ (K)	Cooling power ( $\text{W}/\text{m}^2$ )	DCM
Optimized Grating	+46	271 (350 K)	-0.44
SiO <sub>2</sub> / HfO <sub>2</sub> Multilayer	-4.9	82	1.86
Glass-Polymer Hybrid Metamaterial	-----	>110	-----
PDMS (300 $\mu\text{m}$ )	-6	188	1.86